

Accepted for the publication in the *Astrophysical Journal*

A Deep Chandra Observation of the Oxygen-Rich Supernova Remnant 0540–69.3 in the Large Magellanic Cloud

Sangwook Park

*Department of Astronomy and Astrophysics, Pennsylvania State University, 525 Davey
Laboratory, University Park, PA. 16802, USA*

park@astro.psu.edu

John P. Hughes

*Department of Physics and Astronomy, Rutgers University, 136 Frelinghuysen Road, Piscataway,
NJ. 08854-8019, USA*

Patrick O. Slane

Harvard-Smithsonian Center for Astrophysics, 60 Garden Street, Cambridge, MA. 02138, USA

Koji Mori

*Department of Applied Physics, University of Miyazaki, 1-1 Gakuen Kibana-dai Nishi, Miyazaki,
889-2192, Japan*

and

David N. Burrows

*Department of Astronomy and Astrophysics, 525 Davey Lab., Pennsylvania State University,
University Park, PA. 16802, USA*

ABSTRACT

Using our deep ~ 120 ks *Chandra* observation, we report on the results from our spatially-resolved X-ray spectral analysis of the “oxygen-rich” supernova remnant (SNR) 0540-69.3 in the Large Magellanic Cloud. We conclusively establish the nonthermal nature of the “arcs” in the east and west boundaries of the SNR, which confirms the cosmic-ray electron acceleration in the supernova shock ($B \sim 20\text{--}140 \mu\text{G}$). We report tentative evidence for Fe overabundance in the southern region close to the outer boundary of the SNR. While such a detection would be intriguing, the existence of Fe ejecta is not conclusive with the current data because of poor photon statistics and limited plasma models. If it is verified using deeper X-ray observations and improved plasma

models, the presence of Fe ejecta, which was produced in the core of the supernova, near the SNR’s outer boundary would provide an intriguing opportunity to study the explosive nucleosynthesis and the ejecta mixing in this young core-collapse SNR. There is no evidence of X-ray counterparts for the optical O-rich ejecta in the central regions of the SNR.

Subject headings: ISM: abundances — ISM: individual (SNR 0540–69.3) — supernova remnants — X-rays: ISM

1. INTRODUCTION

The supernova remnant (SNR) 0540–69.3 in the Large Magellanic Cloud (LMC) is well known for its bright central pulsar (PSR B0540–69.3) and its pulsar wind nebula (PWN) which show similar characteristics to those of the Crab. The pulsar and PWN have been extensively studied at many wavelengths (e.g., Middleditch & Pennypacker 1985; Manchester et al. 1993a,b; Gotthelf & Wang 2000; Kaaret et al. 2001; Petre et al. 2007 and references therein). SNR 0540–69.3 is also one of the two known members of “oxygen-rich” SNRs in the LMC. In the optical band, early data of 0540–69.3 showed a ring-like ($\sim 4''$ in radius) [O III] feature around the pulsar/PWN, which is identified as the O-rich ejecta (Mathewson et al. 1980). The spatial and spectral structures of the optical filamentary features in this region were studied using the *Hubble Space Telescope* observations, which revealed the details of the ejecta and the synchrotron nebula (Morse et al. 2006). The filamentary features of the optical line emission were suggested to result from magnetic Rayleigh-Taylor instabilities due to the interaction between the expanding synchrotron nebula and the surrounding ejecta, just like those seen in the Crab (Morse et al. 2006). This central region was also thoroughly studied in infrared (IR) using the *Spitzer Space Telescope* observations (Williams et al. 2008). These observations revealed that the central nebula of 0540–69.3 is analogous to that of the Crab, showing synchrotron emission from the PWN, a complex network of ejecta filaments, and newly formed dust. A progenitor mass of 20–25 M_{\odot} was suggested based on the observed metal ejecta abundances (Williams et al. 2008). The enhanced optical and IR emission most likely originates from the interaction between the PWN and the freely-expanding metal-rich ejecta.

Besides the central pulsar and PWN, the SNR shell produced by the interaction between the blast wave and the surrounding medium was detected in the radio band (Manchester et al. 1993b). The radio spectral index in the outer shell ($\alpha = 0.41$, where $S_{\nu} \propto \nu^{-\alpha}$) is steeper than that in the PWN ($\alpha = 0.25$), which indicated that the shell emission is synchrotron radiation from the shock-accelerated electrons. The age of SNR 0540–69.3 has been estimated to be $\tau \sim 760$ –1660 yr based on various methods such as the pulsar spin-down, the kinematics of the optical ejecta, and the overall dynamics of the ejecta evolutionary models (Seward et al. 1984; Kirshner et al. 1989; Reynolds 1985; Manchester et al. 1993a).

Thermal emission from the SNR shell ($\sim 1'$ in diameter) has been detected in the X-ray band

(Hwang et al. 2001; van der Heyden et al. 2001). The overall SNR morphology of the nearly circular shell with the bright W and faint E regions is consistent with that of the radio images. The bright W filaments are roughly coincident with the patchy [O III] emission feature at $\sim 30''$ W of the pulsar (Mathewson et al. 1980; Seward & Harnden 1994). The detection of these outer filaments, which most likely originate from interactions between the blast wave and ambient medium, in X-rays and radio makes 0540–69.3 observationally distinguished from the Crab in which no emission features from the blast wave significantly beyond the PWN are detected at any wavelengths. Thermal emission from the outer SNR shell is detected prominently in X-rays, and thus X-ray observations of 0540–69.3 provide a unique opportunity to study the ambient and/or circumstellar structures in this SNR as well as the reverse shocked metal-rich ejecta.

Previous X-ray studies of the SNR 0540–69.3 with *Chandra* and *XMM-Newton* produced puzzling results. Enhanced line emission from O, Ne, and Fe was claimed by van der Heyden et al. (2001) based on the *XMM-Newton* RGS data, but was not detected based on the *Chandra* observation (Hwang et al. 2001). The X-ray emission lines detected by *XMM-Newton* in the W regions of the SNR are strongly blue-shifted ($v \sim -2370$ km s $^{-1}$, van der Heyden et al. 2001), which was not evident in the *Chandra* data (Hwang et al. 2001). The *Chandra* data suggested an intriguing possibility of the presence of nonthermal X-ray emitting “arcs” in the E and W boundaries (Hwang et al. 2001), which are reminiscent of the nonthermal filaments of synchrotron radiation from the shock-accelerated cosmic-ray (CR) electrons in several Galactic SNRs such as SN 1006. However, the nature (thermal vs. nonthermal) of these faint arcs could not be determined with the previous *Chandra* data because of the poor photon statistics. The *Chandra* data also detected a hard tail ($E > 3$ keV) in the observed X-ray spectrum which appears to prevail in the eastern *hemisphere* of the SNR (Hwang et al. 2001; Hughes 2001). The origin for the hard tail (a thermal plasma with $kT \sim 5$ keV vs. power law [PL] continuum with $\Gamma \sim 2.7$) was uncertain (Hwang et al. 2001). While the previous *Chandra* and *XMM-Newton* data revealed a number of new properties of SNR 0540–69.3, some results were inconclusive and/or controversial. The uncertainties and discrepancies in the previous X-ray results appear to be caused largely by the poor photon statistics in the *Chandra* data (a 28 ks exposure) and/or the poor angular resolution ($\sim 1'$) of *XMM-Newton* RGS (Hwang et al. 2001; van der Heyden et al. 2001). Motivated by these discrepancies, we performed a deep *Chandra* observation to address the outstanding issues and to reveal the true nature of SNR 0540–69.3.

Here we report the results from the data analysis of our deep 120 ks *Chandra* observation of SNR 0540–69.3. We focus on our spectral analysis of the diffuse X-ray emission features outside of the PWN. The spectral analysis of the PWN will be presented elsewhere. In Section 2, we describe the observations and the data reduction. We present the spectral analysis of the SNR in Section 3. We discuss the results and implications in Section 4, and present a summary in Section 5.

2. OBSERVATIONS & DATA REDUCTION

We observed SNR 0540–69.3 with the Advanced CCD Imaging Spectrometer (ACIS) on board *Chandra X-Ray Observatory* during AO6 (in 2006 February 15–18, ObsIDs 5549, 7270, and 7271). We used the ACIS-S3 for the effective detection of the soft X-ray emission of the SNR. The previous *Chandra* observation of 0540–69.3 (ObsID 119) showed significant photon pileup effects in the central regions of the PWN (Hwang et al. 2001; Petre et al. 2007). To reduce the pileup effects in the PWN as much as possible while covering the entire SNR, we chose a 1/4-subarray of the ACIS. We corrected the spatial and spectral degradation of the ACIS data caused by the charge transfer inefficiency (CTI; Townsley et al. 2000) using the methods developed by Townsley et al. (2002). We applied the standard data screening by status and grade (*ASCA* grades 02346). Since our observation was split into three segments (~ 40 ks exposure for each segment), we performed these data reduction steps on individual observations. The three data sets were then merged into a single event file by re-projecting them onto the ObsID 5549’s tangential plane. After the data reduction, the effective exposure was 114.2 ks. The archival *Chandra* data of 0540–69.3 (ObsID 119) were obtained with a significantly shorter exposure (28 ks), and the results of the data analysis have been published (Hwang et al. 2001; Petre et al. 2007). Since the low photon statistics of these archival data did not significantly enhance the statistics of our new data analysis, we used only our new deep observation in this work.

3. Spectral Analysis

Figure 1a shows an X-ray color image of SNR 0540–69.3. The central region is dominated by emission from the bright pulsar PSR B0540–69.3 and its PWN. The bright X-ray emission from the pulsar results in the trail image running NE-SW (corresponding to the CCD’s read-out direction). We excluded this trail region ($\sim 2''.5$ width) in the spectral analysis. SNR 0540–69.3 is projected on complex diffuse background structures (Hwang et al. 2001). We tested several nearby source-free regions for the background spectrum. Although regions to the S and W of the SNR show generally higher background emission (by $\sim 20\%$ in the total count rates) than regions to the N because of the relatively bright soft background emission ($E < 1.5$ keV) there, the selection of different background regions does not have a significant effect on our SNR spectral analysis. In this work, we use an average background spectrum extracted from four circular regions ($\sim 15''$ in radius) to the NE, NW, SE, and SW of the SNR (Figure 2).

Thanks to the use of the 1/4 subarray of the ACIS-S3, our new observation of SNR 0540–69.3 shows reduced photon pileup effects in the PWN region. Based on simple tests using the event grade distribution and the count rate changes in the SNR between observations in 1999 and 2006, we find that regions with radial distance $R \gtrsim 3''$ from the pulsar are nearly free from pileup effects (Regions within $R \lesssim 2''$ are still significantly piled up.) The O-rich ejecta detected in the optical band shows a shell-like morphology with a radius of $R \sim 4''$ (Mathewson et al. 1980; Morse et al. 2006). Thus,

using the pileup-free data, we can perform a reliable spectral analysis of this region to search for X-ray counterparts for the optical O-rich ejecta. However, the central regions of the SNR, which are spatially coincident with the optical ejecta features, are dominated by the bright PWN in X-rays. We find no evidence for enhanced X-ray emission features from the O He_α and/or O Ly_α lines at $R \sim 4''\text{--}5''$. This result confirms the conclusions inferred by the previous data (Petre et al. 2007). We here concentrate our spectral analysis on the faint E-S regions, bright W filaments, and the faint E arc. In all spectral fits presented in the following sections, we binned each regional spectrum to contain a minimum of 20 counts per energy bin.

3.1. The “Arc” Region

Small arc-like filaments on the E and W boundaries of the SNR were discovered by the previous *Chandra* data (Hwang et al. 2001). As Hwang et al. (2001) noted, this particular morphology and the hard X-ray spectrum of these features raised the intriguing possibility of strong particle acceleration sites at the shock front of 0540–69.3, in analogy to the “bi-polar” nonthermal X-ray filaments in the Galactic historical SNR 1006. In fact, Hwang et al. (2001) suggested that a significant portion of the X-ray emission in these arcs could be nonthermal continuum in origin. However, because of the poor photon statistics (e.g., ~ 190 counts in the arc region in the E boundary), the true nature of these features could not be revealed by the previous *Chandra* data. With a four times deeper exposure, we obtain significantly better photon statistics from these arcs to study the spectral characteristics. We note that the W arc region is projected on the bright thermal emission features of the SNR. Also, the trail image by the pulsar is partially superposed onto the W arc (Figure 1b). The spectral analysis of the W arc is difficult and less useful than the E arc due to these complex environments and the detector artifacts. In fact, our two-component spectral model fits (plane shock + PL) for the W arc result in nearly the same spectral parameters for the hard PL component ($\Gamma \sim 2.4$, $f_{0.5-8 \text{ keV}} \sim 4 \times 10^{-14} \text{ erg cm}^{-2} \text{ s}^{-1}$) as those for the E arc (see below). Because the soft thermal emission dominates the overall W arc spectrum, the best-fit PL parameters are poorly constrained compared to those in the E arc. Thus, we discuss the nature of the arcs based on the spectral analysis of the E arc (the “Arc” region in Figure 2).

The Arc region contains ~ 750 counts and is well-separated from the bright thermal filaments, as well as avoiding contamination by the pulsar trail image. The Arc region shows a featureless X-ray spectrum which can be fitted by a PL model with $\Gamma = 2.42^{+0.26}_{-0.23}$ (uncertainties are with a 90% confidence level, hereafter). We fixed the Galactic absorbing column at $N_{\text{H,Gal}} = 7 \times 10^{20} \text{ cm}^{-2}$ (Dickey & Lockman 1990). We fit the foreground column in the LMC ($N_{\text{H,LMC}} = 6.5^{+1.8}_{-1.5} \times 10^{21} \text{ cm}^{-2}$), assuming LMC interstellar abundances (Russell & Dopita 1992). The X-ray spectrum of the Arc region and the best-fit PL model ($\chi^2/\nu = 39.8/31$) are presented in Figure 3. The plane-parallel shock model with LMC abundances cannot fit the observed spectrum ($\chi^2/\nu = 2.8$). When the individual metal abundances are varied, the fit results in a large column ($N_{\text{H,LMC}} \sim 1.9 \times 10^{22} \text{ cm}^{-2}$) and a high electron temperature ($kT \sim 2.3 \text{ keV}$). The fitted abundances are

negligible for most species except for O (~ 5) and Ca (~ 4 , abundances are with respect to Solar [Anders & Grevesse 1989], hereafter). The fitted LMC column is implausibly large for this location of the LMC. The inferred overabundances for O and Ca are statistically insignificant due to large uncertainties. The best-fit model ($\chi^2/\nu = 35.0/22$) is significantly poorer than the PL model fit. A two-component model (PL + plane shock) indicates only a small contribution ($\sim 5\%$ of the total flux) from the thermal plasma ($kT \sim 0.4$ keV). The PL + plane shock model does not improve the overall fit ($\chi^2/\nu = 36.7/28$). Thus, we conclude that the X-ray emission in the Arc region is dominated by nonthermal PL continuum. The best-fit photon index ($\Gamma \sim 2.4$) is consistent with the typical value for synchrotron radiation by relativistically accelerated electrons in the strong SN shock.

Assuming that synchrotron radiation from the shock-accelerated electrons is responsible for the X-ray and radio emission for the Arc, we fit the observed Arc spectrum with the synchrotron cutoff model (SRCUT, Reynolds 1998; Reynolds & Keohane 1999). We fixed the radio spectral index at $\alpha = 0.41$ as estimated for the entire SNR excluding the central PWN (Manchester et al. 1993b). The best-fit LMC column, $N_{\text{H,LMC}} = 5.7_{-0.9}^{+1.0} \times 10^{21} \text{ cm}^{-2}$, is consistent with that measured by the PL model fit. The fitted synchrotron roll-off frequency is $\nu_{\text{roll}} = 1.0_{-0.4}^{+1.4} \times 10^{17} \text{ Hz}$. Our X-ray spectral analysis indicates that the 1 GHz flux for the radio counterpart is $f_{1\text{GHz}} \sim 0.19 \text{ mJy}$. On the other hand, based on the 1.5 and 5 GHz images (Manchester et al. 1993b), we roughly estimate $f_{1\text{GHz}} \sim 7 \text{ mJy}$ for the Arc region. This radio flux is significantly larger than our estimate from the X-ray spectral fit, which suggests that the radio spectral index may not be uniform across the SNR. Thus, we repeated the SRCUT model fit of the Arc region by fixing $f_{1\text{GHz}} = 7 \text{ mJy}$ while varying the radio spectral index α . The best-fit parameters are $N_{\text{H,LMC}} = 5.7_{-0.8}^{+1.0} \times 10^{21} \text{ cm}^{-2}$, $\nu_{\text{roll}} = 2.1_{-1.2}^{+4.7} \times 10^{17} \text{ Hz}$, and $\alpha = 0.62 \pm 0.01$. The best-fit radio spectral index is not unusual for Galactic shell-type SNRs (Green 2009). Based on the PL and SRCUT model fits, the observed X-ray flux (absorbed) of the Arc is $f_{0.5-8 \text{ keV}} \sim 3.7 \times 10^{-14} \text{ erg cm}^{-2} \text{ s}^{-1}$. At the distance of $d = 50 \text{ kpc}$ for the LMC ($d = 50 \text{ kpc}$ for SNR 0540–69.3 is assumed in this paper hereafter), the unabsorbed X-ray luminosity is $L_{0.5-8 \text{ keV}} \sim 1.7 \times 10^{34} \text{ erg s}^{-1}$. The best-fit model parameters for the Arc region are summarized in Table 1.

We note that the estimated absorbing column to the Arc can be reliably assumed for other regions of SNR 0540–69.3 because it is measured by straightforward models (PL and SRCUT) of the simple continuum-dominated spectrum. In fact, our spectral fits for the central region ($R = 4''\text{--}5''$, the “ring” region in Figure 2) also indicate $N_{\text{H,LMC}} = 6.0 \pm 0.5 \times 10^{21} \text{ cm}^{-2}$. This central region is close to the PWN, in which the observed spectrum is dominated by the simple PL continuum and provides significant photon statistics (~ 3600 counts), while the pileup effects are convincingly ruled out. We find that other regional spectral analysis requires more complicated thermal spectral modelings which result in less reliable estimates of $N_{\text{H,LMC}}$ (e.g., Hwang et al. 2001). Thus, based on the results from the spectral analysis of the Arc region, we fix the LMC column at $N_{\text{H,LMC}} = 6 \times 10^{21} \text{ cm}^{-2}$ in the following spectral analysis of the SNR. This $N_{\text{H,LMC}}$ value is somewhat higher than those estimated/adopted in previous works ($N_{\text{H}} \sim 4\text{--}5 \times 10^{21} \text{ cm}^{-2}$, e.g., Kaaret et al.

2001; Petre et al. 2007). The higher $N_{\text{H,LMC}}$ is justified by the realistic assumption of the LMC abundances in our absorption model, while the previous works assumed the Solar abundances. Our $N_{\text{H,LMC}}$ is fully consistent with that estimated by Serafimovich et al. (2004) who also assumed the LMC abundances for the absorbing column by the LMC.

3.2. Faint East Region

The eastern half of the SNR is generally faint, and X-ray emission appears to originate from a hot plasma of the electron temperature $kT \sim 5$ keV (Hwang et al. 2001). However, the previous results on the faint eastern regions were rather preliminary based on a simple spectral analysis of the integrated spectra from the “inner” and “outer” regions of the entire eastern half of the SNR. The inner parts of the eastern half of the SNR could be substantially contaminated by scattered photons from the bright pulsar and PWN. The outer regions of the eastern half show an intensity variation with a relatively bright emission in the north. Furthermore, our new deep *Chandra* data reveal that X-ray emission near the southern boundary, which was included in the “outer east” region by Hwang et al. (2001), is spectrally-soft (Figure 1a). Thus, we carefully re-analyze the faint E region excluding the relatively bright N regions and the spectrally-soft S regions. We also exclude the central regions of $R \lesssim 20''$ to avoid the contamination from the pulsar and PWN as much as possible (our radial cut to remove the PWN is more conservative than that by Hwang et al. [2001] who excluded regions of $R \leq 7''$.) Based on our MARX¹ simulations of the pulsar/PWN of 0540–69.3, we estimated that the contamination by scattered photons from the pulsar/PWN due to the broad PSF wings of the mirror is ~ 20 – 30 % in the observed 3–7 keV band flux for the “E” region (as shown in Figure 2). In these simulations, we assumed our observed ACIS image of the PWN ($R \leq 4''$) with a PL spectrum of $\Gamma = 2$ and the 1–10 keV band flux of 3.2×10^{-11} erg cm⁻² s⁻¹ (Hirayama et al. 2002). The spectrum of the scattered photons is hard (a PL with $\Gamma \sim 0.25$) at these large radial distances of $R \sim 20''$ – $30''$ from the pulsar. Thus, this instrumental artifact contaminates primarily at $E \gtrsim 5$ keV. We fixed this scattered photon flux spectrum in the spectral model fits of the E region. (The broad PSF wing flux was estimated in the annular region of $R = 20''$ – $30''$ using our MARX simulations, and was then normalized for the area of the E region. This normalized flux and the best-fit PL photon index for the scattered photon spectrum were fixed in the spectral model fits of the E region.)

The X-ray spectrum of the E region includes ~ 1600 counts. The overall spectral characteristics are consistent with those shown for the “outer east” region in Hwang et al. (2001): the soft band spectrum evidently shows X-ray line emission features, and the hard tail extends to $E > 4$ keV. Initially, we fit the observed spectrum with a non-equilibrium ionization (NEI) plane-shock model (Borkowski et al. 2001; *vpshock* in conjunction with the NEI version 2.0 in the XSPEC) that is based on ATOMDB (Smith et al. 2001). We use an augmented version of this atomic database

¹<http://space.mit.edu/CXC/MARX/>

to include inner-shell processes and updates of the Fe L-shell lines, whose effects are significant in highly under-ionized plasma spectrum, but are not accounted for in the current XSPEC NEI version 2.0.² This model includes inner-shell Fe L lines from Na-like Fe ion at $E = 725.15, 727.06$, and 738.98 eV which are critical to properly fit the broad Fe L line complex-like feature in the $0.7\text{--}0.8$ keV band (see Section 3.3), but were not included in the standard XSPEC NEI version 2.0. Thus, although it is still incomplete, our NEI model is the most reliable one that is currently available to the astronomical community to fit highly under-ionized plasma. We use this latest NEI model in the spectral analysis of thermal X-ray emission throughout this work. We fixed the individual metal abundances at the LMC values (Russell & Dopita 1992). We fixed the LMC column at $N_{\text{H,LMC}} = 6.0 \times 10^{21} \text{ cm}^{-2}$ based on the results from the spectral analysis of the Arc region (see Section 3.1). Although the overall spectrum can be fitted by a $kT \sim 9$ keV thermal plasma, the fit is statistically rejected ($\chi^2/\nu \sim 2.1$) because of the large residuals in the soft band ($E \sim 0.5\text{--}2$ keV). When the LMC column is varied, the fit improves, but is still relatively poor ($\chi^2/\nu \sim 1.5$). The fitted $N_{\text{H,LMC}}$ ($\sim 2.5 \times 10^{21} \text{ cm}^{-2}$) is significantly lower than that estimated for the Arc. Thus, the single plane-shock models with the LMC abundances are not appropriate to fit the observed spectrum.

The fit improves to be statistically acceptable when the individual metal abundances are varied. We attempted to fit abundances for O, Ne, Mg, Si, S, Ar, Ca, and Fe while other elements (He, C, N, and Ni) were fixed at the LMC abundances. We found that only O and Ne abundances significantly affected the fit. Thus, we varied O and Ne abundances and fixed other elements at the LMC values ($\chi^2/\nu = 64.8/55$, Figure 4a and Table 2). The best-fit electron temperature is $kT = 3.08_{-0.92}^{+0.63}$ keV with a low ionization timescale of $n_e t \sim 0.60 \times 10^{10} \text{ cm}^{-3} \text{ s}$. We fixed the LMC column at $N_{\text{H,LMC}} = 6.0 \times 10^{21} \text{ cm}^{-2}$ in this fit. The best-fit abundances for O ($= 0.03_{-0.01}^{+0.02}$) and Ne ($= 0.09_{-0.03}^{+0.04}$) are low, showing no evidence for metal-rich ejecta. When the LMC column was varied, the fit does not statistically improve ($\chi^2/\nu = 62.8/54$), and the best-fit $N_{\text{H,LMC}}$ ($= 1.2 \times 10^{22} \text{ cm}^{-2}$) is unreasonably high for the LMC. The best-fit abundances for O (~ 0.3) and Ne (~ 0.2) are similar to those of the LMC, but are poorly constrained. Thus, the E region spectrum can be described by a single plane shock model in which O and Ne abundances are lower than the LMC values.

Alternatively, we fit the spectrum with a two-component plane shock model with the metal abundances fixed at the LMC values for both components. The LMC column was fixed at $N_{\text{H,LMC}} = 6.0 \times 10^{21} \text{ cm}^{-2}$ for both components. The fit is statistically acceptable ($\chi^2/\nu = 60.7/54$, Table 2). The best-fit electron temperatures are $kT_{\text{soft}} = 1.72_{-0.35}^{+1.63}$ and $kT_{\text{hard}} = 3.20_{-1.06}^{+2.55}$ keV. The soft component emission originates from an under-ionized thermal plasma ($n_e t_{\text{soft}} \sim 3.4 \times 10^{10} \text{ cm}^{-3} \text{ s}$). The ionization timescale for the hard component is unconstrained. We also considered the hard tail of the observed X-ray spectrum to be nonthermal in origin, and thus repeated the two-component

²The augmented APEC atomic data have been provided by K. Borkowski. The relevant discussion on these detailed plasma model issues has been presented in Badenes et al. (2006).

model fits by replacing the hard component plane shock model with a PL. The best-fit PL photon index is $\Gamma = 2.23 \pm 0.33$, and the electron temperature of the thermal component is estimated to be $kT = 1.72_{-0.69}^{+2.38}$ ($\chi^2/\nu = 56.2/55$, Table 2). The modeled PL spectrum is consistent with that for typical synchrotron radiation from the shock-accelerated electrons. In fact, synchrotron radiation observed in the Arc region shows a similar PL spectrum with $\Gamma = 2.4$ (Section 3.1).

3.3. Soft South Region

The faint southern boundary region, which is distinctively red in Figure 1a, is spectrally soft. This has not been recognized by previous data, and our new *Chandra* data reveal this feature. We extracted ~ 900 counts from this region (the “S” region in Figure 2). The observed X-ray spectrum shows line emission features at $E \sim 0.6\text{--}1.5$ keV as well as the hard tail at $E > 3$ keV (Figure 4b). We estimated the effects by the scattered photons from the pulsar and PWN due to the broad PSF wings of the mirror using the same methods described in Section 3.2. The contamination by scattered photons from the pulsar and PWN is estimated to be $\sim 20\%$ in the 3-7 keV band in this region. We fixed the PL component of the scattered photons (with the flux normalized for the area of the S region) in the spectral fits of the S region. Initially, we fit the spectrum with a single temperature NEI plane-shock model. We fixed the individual metal abundances at the LMC values, and also fixed the LMC column at $N_{\text{H,LMC}} = 6.0 \times 10^{21} \text{ cm}^{-2}$. The best-fit model ($kT \sim 1.14$ keV and $n_e t \sim 0.9 \times 10^9 \text{ cm}^{-3} \text{ s}$) is statistically poor ($\chi^2/\nu = 1.6$). Varying $N_{\text{H,LMC}}$ does not improve the fit ($N_{\text{H,LMC}} \sim 5.1 \times 10^{21} \text{ cm}^{-2}$, $\chi^2/\nu = 1.5$). The poor fits are primarily caused by residuals at $E \sim 0.7\text{--}0.9$ keV. Because the residual line features at $E \sim 0.7\text{--}0.9$ keV appear to be the Fe L line complex, we varied the Fe abundance. The best-fit model ($kT \sim 1.20_{-0.60}^{+0.19}$ keV and $n_e t = 0.33_{-0.07}^{+0.11} \times 10^{10} \text{ cm}^{-3} \text{ s}$) statistically improves ($\chi^2/\nu = 32.9/33$, Figure 4b and Table 2), and suggests overabundant Fe ($= 18.5_{-13.7}^{+59.5}$). We similarly attempted to vary O and/or Ne abundances, and found that O and Ne overabundances are not required to improve the fit. When O and/or Ne abundances are fitted with the Fe abundance fixed at the LMC value, the best-fit model fit clearly shows residuals at $E \sim 0.7\text{--}0.9$ keV, which suggests that the emission features in the 0.7-0.9 keV band are likely dominated by the broad Fe L line complex. Varying $N_{\text{H,LMC}}$ results in nearly the same spectral parameters with no statistical improvement ($\chi^2/\nu = 32.3/32$): The Fe overabundance is still suggested ($\text{Fe} = 17.3_{-13.1}^{+48.4}$) with similar kT (~ 1.37 keV) and $N_{\text{H,LMC}}$ ($\sim 5.6 \times 10^{21} \text{ cm}^{-2}$).

For completeness, we attempted two-temperature plane-shock models to fit the S region spectrum. $N_{\text{H,LMC}}$ was fixed as above, and the metal abundances were also fixed at the LMC values. The best-fit model ($\chi^2/\nu = 31.4/31$) suggests a high temperature plasma ($kT_{\text{hard}} > 2.4$ keV) in addition to the soft component ($kT_{\text{soft}} \sim 0.35$ keV). Because the single temperature model fit suggested an Fe overabundance, we tested whether the Fe overabundance is required in the two component model. When the Fe abundance is varied, an Fe overabundance (> 1.2) is suggested, while other spectral parameters remain generally consistent with those estimated with the LMC abundances ($\chi^2/\nu = 25.8/30$). Nonetheless, these two-component models do not statistically im-

prove the fit, compared to the single component models. Based on the single plane shock model fits, the enhanced Fe abundance appears to be required to adequately fit the observed spectrum of the S region. However, the statistical uncertainties on the Fe abundance measurements are large (i.e., the Fe overabundance is a $\sim 2\text{--}3\sigma$ detection above the LMC value). Also, the two-temperature plasma models may equally fit the observed spectrum without overabundant Fe. Thus, while the Fe overabundance is suggested in the S region, a firm conclusion may not be drawn with the current data.

3.4. Bright West Regions

In contrast to the faint E and S regions, the western parts of the SNR show bright filamentary emission features (Figure 1a). Hwang et al. (2001) revealed that the bright western filaments, except for the small region near the outer boundary in the direction opposite to the E arc, are dominated by soft X-ray emission from thermal plasma with $kT \sim 0.5\text{--}1$ keV. The previous *Chandra* data indicated no evidence for enhanced metal abundances in the bright western regions (Hwang et al. 2001), while the *XMM-Newton* RGS data suggested enhanced emission from Fe L and Ne K lines (van der Heyden et al. 2001). Results from our spectral analysis of the western filaments are generally consistent with those by Hwang et al. (2001). We here present our spectral analysis of two representative regions: the “SW” and “NW” regions (Figure 2). We choose the SW region because it shows bright thermal emission at the outer boundary, likely representing the blast wave with good photon statistics. The NW region includes a significant fraction of the hard emission ($kT \sim 5$ keV) among the western filaments (besides the regions of the candidate nonthermal filament at the outer boundary, Hwang et al. 2001). In the spectra of the SW and NW regions, the contamination by the scattered hard X-ray photons from the pulsar and PWN is negligible thanks to the small extraction area. Thus, we do not include the PL component of the broad PSF wings in the spectral fits of these regions.

The SW region spectrum (~ 2200 counts) is presented in Figure 4c. The overall spectrum can be fitted by a single component plane-shock model ($kT \sim 0.74$ keV, $n_e t \sim 5.3 \times 10^{10} \text{ cm}^{-3} \text{ s}$, $\chi^2/\nu = 74.5/54$). We fixed the LMC column at $N_{\text{H,LMC}} = 6.0 \times 10^{21} \text{ cm}^{-2}$, and the individual metal abundances at the LMC values. When $N_{\text{H,LMC}}$ was fitted, the best-fit value ($N_{\text{H,LMC}} \sim 6.9 \times 10^{21} \text{ cm}^{-2}$) is similar to that estimated from the Arc, and the overall fit does not improve ($\chi^2/\nu = 74.0/53$). Varying the individual abundances results in the LMC-like abundances ($\sim 0.1\text{--}0.3$) without a significant improvement in the fit ($\chi^2/\nu = 60.8/49$) based on an F-test (F-probability ~ 0.07). There is no evidence for the presence of a hard component ($E \gtrsim 3$ keV) or metal overabundances in this region. The best-fit spectral parameters assuming the LMC abundances are summarized in Table 2.

For the NW region spectrum (~ 2800 counts), a single plane-shock model fit with the fixed $N_{\text{H,LMC}}$ and the LMC abundances is not acceptable ($\chi^2/\nu \sim 2.0$). When the LMC column was fitted, a $\sim 50\%$ higher column ($N_{\text{H,LMC}} = 9.1^{+1.5}_{-1.0} \times 10^{21} \text{ cm}^{-2}$, $kT \sim 1$ keV, $\chi^2/\nu \sim 1.6$) is implied.

However, the observed spectrum of this region is nearly identical to that of SW region in the soft energy band ($E \lesssim 1$ keV, Figure 4), in which the large foreground absorption in the NW region, if it exists, should significantly affect the observed spectral shape. Then, we varied the metal abundances (with $N_{\text{H,LMC}} = 6.0 \times 10^{21} \text{ cm}^{-2}$), which results in a significantly improved fit ($\chi^2/\nu = 80.1/65$, Figure 4d). The best-fit abundances are low (~ 0.05 – 0.2) showing no evidence for metal-rich ejecta. The fitted spectral parameters are summarized in Table 2. Since the hard spectral component with $kT \sim 5$ keV was suggested in this region in the previous work (Hwang et al. 2001), we, for completeness, attempted a two-component plane-shock model fit for the NW region. In this fit, we fixed $N_{\text{H,LMC}} = 6.0 \times 10^{21} \text{ cm}^{-2}$ and the abundances at the LMC values. The best-fit model indicates $kT_{\text{soft}} \sim 0.6$ keV and $kT_{\text{hard}} \sim 1.4$ keV ($\chi^2/\nu \sim 1.0$). Although the two temperature shock model can adequately fit the observed spectrum, the electron temperature for the hard component is significantly lower than that implied in the E region. Varying $N_{\text{H,LMC}}$ and the abundances does not affect these results. The best-fit spectral parameters for the two component model are also summarized in Table 2.

4. Discussion

4.1. Nonthermal Filament

Using our deep *Chandra* observation, we firmly establish the nonthermal nature of the Arc in the E boundary of SNR 0540–69.3. The observed X-ray spectrum is well fitted by a PL with $\Gamma = 2.42$, which is typical for synchrotron radiation from relativistically accelerated electrons in the strong shock. The contribution from underlying thermal emission is estimated to be small ($\sim 5\%$ of the total flux, if exists). Assuming the synchrotron origin, our SRCUT model fits indicate that the roll-off frequency between the radio and X-ray bands is $\nu_{\text{roll}} \sim 1\text{--}2 \times 10^{17} \text{ Hz}$. The *Chandra* image shows that the Arc consists of several substructures with various widths and brightness. Based on these filamentary features, we estimate the widths of the Arc to be in a range of $\sim 1''$ – $2''.8$ (FWHM) which correspond to a physical size of ~ 0.3 – 0.7 pc. SNR 0540–69.3 may be in a free-expansion phase at the age of $\tau \sim 1000$ yr (e.g., Hwang et al. [2001] and references therein). Then, the angular distance of the Arc to the SNR center ($\sim 35''$ corresponding to a physical distance of ~ 8.5 pc) suggests a time-average shock velocity $v_s \sim 8300 \tau_1^{-1} \text{ km s}^{-1}$, where τ_1 is the SNR age in units of 1000 yr. Assuming the Sedov phase, $v_s \sim 3300 \tau_{1000}^{-1} \text{ km s}^{-1}$ is implied. These velocities are in plausible agreement with the estimated shock velocities ($v_s \sim 2000$ – 9000 km s^{-1}) for the SNR in a free-expansion or a Sedov phase, based on the spectral analysis of the thermal component emission for the E region (Section 4.2). The estimated widths of the Arc filaments and these shock velocities ($v_s \sim 2000$ – 9000 km s^{-1} for the E region) imply the synchrotron loss time $\tau_{\text{loss}} \sim \omega v_s^{-1} r \sim 160$ – 2700 yr, where ω is the advection distance of the downstream electrons or the physical width of the filament, and r is the compression ratio in the shock. In this estimate, we assumed $r \sim 5$ – 8 for an efficient particle acceleration (e.g., Ellison et al. 2007).

The peak frequency of a synchrotron emitting electron is $\nu_p = 1.8 \times 10^{18} E_e^2 B_\perp$ Hz, where B_\perp is the magnetic field component perpendicular to the velocity vector of the electron, and E_e is the electron energy. For $\nu_p \sim 3 \times 10^{17}$ Hz (or the photon energy ~ 1.3 keV) representing typical X-ray photons as observed in the Arc spectrum, the corresponding electron energy $E_e = 0.4 B_\perp^{-\frac{1}{2}}$ erg implies $B_\perp = 136 \eta_{\text{oss}}^{-\frac{2}{3}}$ G. For the estimated $\eta_{\text{oss}} \sim 160\text{--}2700$ yr, we derive $B_\perp \sim 7\text{--}46 \mu\text{G}$. Considering a geometrical projection effect in estimating the widths of the filaments, the actual B field is likely larger than these estimates. For instance, the observed filament width would be overestimated by a factor of ~ 5 assuming a spherical shock with an exponential emission profile (Ballet 2006). Then, $B \sim 20\text{--}140 \mu\text{G}$ are estimated. The maximum electron energy is $E_{e,\text{max}} = 2.5 \times 10^{-7} \nu_{\text{roll}}^{\frac{1}{2}} B_{\mu\text{G}}^{-\frac{1}{2}}$ TeV $\sim 7\text{--}25$ TeV. The estimated B field is roughly an order of magnitude higher than typical LMC interstellar fields ($B \sim 4 \mu\text{G}$, Gaensler et al. 2005), indicating a strong magnetic field amplification in the SNR shock. It was suggested that the presence of ordered magnetic fields in the LMC (and in other young/irregular galaxies) could have originated from the CR-driven dynamo due to recent SN activity rather than the standard galactic rotational dynamo mechanism (Gaensler et al. 2005). The detection of synchrotron emission by the shock-accelerated relativistic electrons in SNR 0540–69.3, which is located in the LMC’s largest active star-forming region 30 Doradus, provides support for the presence of such a population of relativistic particles in the LMC. These spectral characteristics of the nonthermal emission, the morphology of the thin filamentary features in opposite sides of the SNR, and the young age of ~ 1000 yr for SNR 0540–69.3 are similar to those observed in Galactic SNRs 1006 (e.g., Bamba et al. 2003) and G330.2+1.0 (Park et al. 2009). While this general scenario is plausible, we note that the quality of the current data is somewhat limited, and thus our simplified interpretations of the magnetic field amplification need to be taken with a caution. For instance, the detailed spatial substructures of the Arc is complex rather than a spherical shell. Thus, our simple geometrical correction may not be fully justified, and the true uncertainties on the magnetic field measurements could be significantly larger. High angular resolution X-ray imaging data with deeper observations will be required to conclusively reveal the true nature of the magnetic field structure in this SNR.

4.2. Thermal Emission and Metal Abundances

Based on the spectral analysis of the E region, we confirm the presence of a hard component ($E > 3$ keV) in 0540–69.3. Two-component spectral model fits indicate that this hard component emission can be described either by a hot gas ($kT \sim 3$ keV) or a PL ($\Gamma \sim 2.2$). With the current data, it is difficult to statistically discriminate the thermal or nonthermal origin for the hard X-ray emission in the E region. Although the PL component is similar to that for synchrotron radiation in the Arc region ($\Gamma \sim 2.4$), there is no evidence for thin filamentary features which would have been anticipated along the outer boundary of the E region, had the hard X-ray emission originated from the shock accelerated relativistic electrons in highly amplified magnetic fields just behind the shock front. However, we note that SNR 0540–69.3 is significantly more distant than the Galactic SNRs that show thin nonthermal filaments. If the E region of 0540–69.3 consisted of a nest of

thin filaments as observed in the Galactic nonthermal SNR G347.3–0.5, it could be seen largely as a faint smooth rim except for the brightest filaments in the Arc region. Thus, the nonthermal interpretations for the hard component emission in the E region are not clear with the current data. On the other hand, the hard tail of the E region spectrum can be described by a hot gas of $kT \sim 3$ keV (either by a single or two component shock model fits). The presence of this hot plasma is plausible in young SNRs. Although a nonthermal origin for the hard X-ray emission in the E region cannot be ruled out with the current data, we here, for simplicity, discuss the nature of the E regional spectrum assuming a thermal origin.

Based on the best-fit volume emission measure ($EM = n_e n_H V = 1.74 \times 10^{57} \text{ cm}^{-3}$), estimated by the simple one-component plane-shock model fit, we derive the post-shock electron density $n_e \sim 1.44 f^{-\frac{1}{2}} \text{ cm}^{-3}$, where f is the volume filling factor of the X-ray emission. In this estimate, we assumed $n_e = 1.2n_H$ (where n_H is the H number density). We also assumed the X-ray-emitting volume $V \sim 1.0 \times 10^{57} \text{ cm}^3$ for the E region with an *average* path-length of ~ 2.4 pc along the line of sight, corresponding to the angular thickness of the E region ($\sim 10''$) at the distance of $d = 50$ kpc. The two-temperature model implies $n_e \sim 0.67$ and $1.38 f^{-\frac{1}{2}} \text{ cm}^{-3}$ for the soft and the hard component, respectively. These estimated post-shock n_e are several times lower than those measured in the bright W regions (see below). The estimated ionization timescales ($n_e t \sim 0.6\text{--}3 \times 10^{10} \text{ cm}^{-3} \text{ s}$) indicate the ionization ages $t \sim 130\text{--}1600$ yr depending on models. The swept-up mass in this region, $M_{\text{sw}} = n_H m_p V$ (where m_p is the proton mass), is estimated to be small ($M_{\text{sw}} \sim 1.0\text{--}1.4 f^{\frac{1}{2}} M_\odot$), which is consistent with the shock propagating through a low-density medium in a young SNR.

In contrast, the X-ray spectrum in the bright W regions can be fitted by thermal plasmas with relatively low electron temperatures ($kT \sim 0.5\text{--}1.5$ keV). These spectra also imply low LMC-like metal abundances. Thus, the bulk of X-ray emission in the W portions of the SNR originates from the shocked interstellar/circumstellar medium. Based on the fitted EM , we estimate the post-shock n_e for the SW and NW regions. In these calculations, we adopt the same method as above. For the SW region, we use the X-ray emitting volume $V \sim 9 \times 10^{55} \text{ cm}^3$, assuming the path-length of ~ 1 pc along the line of sight. The estimated post-shock electron density is $n_e \sim 5.6 f^{-\frac{1}{2}} \text{ cm}^{-3}$. For the NW region, we assume $V \sim 5 \times 10^{55} \text{ cm}^3$ for the path-length of ~ 0.8 pc along the line of sight. The estimated density is $n_e \sim 6.8\text{--}12.3 f^{-\frac{1}{2}} \text{ cm}^{-3}$ depending on models. The blast wave is encountering several times denser ambient medium in western regions than in eastern regions. While the surrounding density is significantly different between E and W sides of the SNR, the overall radial extent is nearly symmetric in E-W as well as in N-S. We speculate that the ambient density is higher in W, and that the blast wave has probably entered the dense medium there recently. Although the HI map of the LMC (Kim et al. 1998) shows that SNR 0540–69.3 is in fact surrounded by relatively bright HI filaments, these HI filaments are primarily located in N and E sides of the SNR. The bright W shell is not detected in the mid-IR (Williams et al. 2008). On the other hand, Hwang et al. (2001) noted that the CO map of the LMC (Cohen et al. 1988) shows molecular clouds to W of the SNR. However, the low-resolution of the CO map ($\sim 8.8'$) does

not allow one to determine whether the CO clouds are close enough to the SNR to account for the higher implied density in the western filaments. Alternatively, the dense material in the W regions of the SNR might be a relic structure of the stellar winds from the massive progenitor. In this scenario, however, the stellar winds must be highly asymmetric between E and W, which is difficult to reconcile with the winds from a 20–25 M_{\odot} progenitor in the red supergiant phase. High-sensitivity, high-resolution radio observations of 0540–69.3 regions would be useful to study the structures of the surrounding medium and its interactions with the SNR, which may help reveal the origin of the bright W shell of the SNR.

If the SNR is in the adiabatic phase, we can derive the Sedov parameters of the SNR using the results of our spectral analysis. We attempt these estimates using the characteristic E region with a representative electron temperature of $kT = 3$ keV. Assuming an electron-ion temperature equilibrium, this temperature implies a shock velocity $v_s \sim 1600$ km s $^{-1}$. However, the assumed electron-ion temperature equilibrium is unlikely established for $v_s \gtrsim$ several 10^2 km s $^{-1}$ (Ghavamian et al. 2007). Thus, ~ 1600 km s $^{-1}$ may only be considered as a lower limit. The radial distance from the pulsar to the outer boundary in the E region is $\sim 30''$ corresponding to ~ 7.3 pc, and thus the Sedov age of $\tau_{\text{sed}} < 1800$ yr are estimated for $v_s > 1600$ km s $^{-1}$. This SNR age limit is in good agreement with the previously estimated SNR ages of ~ 760 – 1660 yr. Alternatively, the SNR might still be in the free-expansion phase (Hwang et al. 2001), especially in the eastern parts where the density is low. Assuming the free-expansion phase, the shock velocity should be $v_s \sim 7150 \tau_1^{-1}$ km s $^{-1}$. If we take $\tau_{\text{SNR}} \sim 800$ and 1800 yr as *lower* and *upper limits* for the SNR age appropriate for the spectral parameters derived in the E region, the corresponding shock velocities are $v_s \sim 4000$ – 9000 and 1600 – 3600 km s $^{-1}$ for a free-expansion and a Sedov phase, respectively. On the other hand, in the SW region, the electron temperature of $kT = 0.74$ keV implies $v_s > 800$ km s $^{-1}$. The radial distance from the SNR center to the SW boundary is also $\sim 30''$, and thus $\tau_{\text{sed}} < 3600$ yr is estimated. While this age range is broadly consistent with the previous estimates, the derived upper limit on the SNR age is larger than that estimated in the E region. Considering the fact that the angular extent is similar between the E and W boundaries, the large Sedov age estimated in western regions may support that the blast wave has recently entered a dense medium in western regions as discussed above.

The spectrally-soft emission in the S region appears to be caused by enhanced emission from the Fe L line complex (the one-shock model fits) and/or the low temperature of the plasma (the two-shock model fits). A low electron temperature ($kT \sim 0.35$ keV) for this region is implied by the two-component shock model fits. This temperature is ~ 5 – 10 times lower than those estimated in the E region, which could suggest a significantly higher density and thus substantial brightening in the X-ray intensity in the S region compared with its surroundings, unless the low temperature component originates from small clumpy material that may not be resolved by the current data. However, the overall X-ray emission in the S region is faint with no evidence for large density and high X-ray intensity, which is generally not consistent with the inferred low temperature. In the two-shock model fits, the existence of the hard component ($kT > 2.4$ keV) is not firmly conclusive

due to the limited photon statistics (only ~ 40 source counts at $E > 3$ keV). In fact, the one- and two-shock model fits are statistically indistinguishable (Section 3.3), and the presence of the two characteristic plasma components may not be convincingly justified in the current data.

The single shock model fit suggests Fe overabundance in the S region. Although the detection of the Fe overabundance in the S region is not conclusively established in the current data, if true, the suggested candidate Fe-rich ejecta near the southern outer boundary of the core-collapse SNR is intriguing. The presence of the Fe overabundance in the S region would imply that the Fe-rich ejecta created at the deepest core of the massive progenitor has been expelled out to the outermost boundary of the SNR. Such a case has been detected in the young Galactic O-rich SNR Cas A (e.g., Hughes et al. 2000, Hwang & Laming 2003). Although this general scenario is intriguing, a firm detection of the Fe ejecta in the S region is required before discussing conclusive and extensive interpretations of this candidate Fe ejecta. High photon statistics with deeper X-ray observations and improved NEI models to accurately account for the significantly under-ionized Fe L lines are required to perform a quantitative abundance study of this soft feature in the S region, and thus to reveal the true nature of this candidate Fe ejecta.

We do not find evidence for enhanced line emission from Ne and Fe in the bright W regions. This is inconsistent with the results reported by van der Heyden et al. (2001) using the *XMM-Newton* RGS data (van der Heyden et al. 2001), and the discrepancy remains unanswered. Van der Heyden et al. (2001) claimed moderate overabundances (by a factor of ~ 2 – 3) in Ne and Fe relative to the O abundance in the W regions, without quoting uncertainties. We note that our *Chandra* data hint for less abundant O than Ne and Fe (e.g., in the bright NW region, we estimate the O abundance is $\sim 20\%$ of the LMC value, while the Fe abundance is $\sim 50\%$ of the LMC). Thus, we speculate that *high abundances* for Fe and Ne relative to O based on the XMM-Newton data could have been due to low-abundant O rather than the enhanced Ne and Fe. Finally, we find no evidence for the O-rich ejecta corresponding to the optical ring of [O III] enhancements close to the PWN. For the annular region of $R = 4''$ – $5''$ (the “ring” region in Figure 2), the observed X-ray spectrum can be fitted by a PL model with $\Gamma = 2.39 \pm 0.09$ ($N_{\text{H,LMC}} = 6.0 \pm 0.5 \times 10^{21} \text{ cm}^{-2}$, $\chi^2_\nu = 163.3/123$). We place a 3σ upper limit of $f < 5.2 \times 10^{-16} \text{ erg cm}^{-2} \text{ s}^{-1}$ ($= 5.0 \times 10^{-7} \text{ photons cm}^{-2} \text{ s}^{-1}$) for the O Ly α line flux.

5. Summary

We performed a deep ~ 120 ks *Chandra* observation of the O-rich SNR 0540–69.3 in the LMC. We conclusively establish the nonthermal nature of the “arc” in the E boundary of the SNR. The observed X-ray spectrum shows a PL continuum ($\Gamma \sim 2.4$), indicating synchrotron radiation from the shock-accelerated relativistic electrons. Thus, CR electron acceleration is evidently effective in the shock front of this young SNR. Assuming that synchrotron radiation is responsible for the observed X-ray and radio emission in this nonthermal filament, we estimate a roll-off frequency of $\nu_{\text{roll}} \sim 1$ – 2×10^{17} Hz. From our estimates of the shock velocities ($v_s \sim 2000$ – 9000 km s^{-1}), the

physical width of the filament, and the observed spectral shape, we derive post-shock magnetic fields $B \sim 20\text{--}140 \mu\text{G}$. The maximum electron energy is estimated to be $E_{\text{e,max}} \sim 7\text{--}25 \text{ TeV}$.

We confirm the presence of the hard component emission in this young SNR primarily in the faint eastern regions. The hard component spectrum can be described either by a hot gas with $kT \sim 3 \text{ keV}$ or a PL with $\Gamma \sim 2.2$. It is difficult to discriminate the origin of the hard component (thermal vs. nonthermal) because of the low photon statistics in the current data. If the hard X-ray emission is nonthermal, the estimated PL photon index suggests synchrotron radiation for its origin, which is similar to that detected in the Arc region. If the hard emission is thermal, the hot gas implies an ambient density of $n_0 \sim 0.17\text{--}0.35 \text{ cm}^{-2}$ which is several times lower than that estimated in the western regions ($n_0 \sim 1.4\text{--}3 \text{ cm}^{-2}$). The W regions are dominated by bright soft filamentary emission features representing the shocked high density medium of lower electron temperatures ($kT \sim 0.5\text{--}1.5 \text{ keV}$). Metal abundances in the W regions are low ($\lesssim 0.3$), indicating interstellar and/or circumstellar origins rather than metal-rich stellar ejecta. Our spectral analysis of thermal X-ray emission features indicates high shock velocities ($v_s \sim 2000\text{--}9000 \text{ km s}^{-1}$) which are usually expected in young SNRs where particle acceleration is efficient.

In the S boundary of the SNR, we detect a faint emission feature which shows a distinctively soft X-ray spectrum compared to the surrounding regions. The Fe abundance in this region appears to be enhanced, although the detection of the Fe overabundance is not conclusive because of the low photon statistics in the current data and the incomplete Fe L line models for highly under-ionized thermal plasma. If it is confirmed by follow-up high statistics data and improved NEI models, the suggested Fe-rich ejecta candidate at the outer boundary of the SNR is intriguing. It would be the detection of Fe ejecta created in the deepest core of the SN and subsequently expelled to nearly the outer blast wave just like those seen in Cas A. Deeper *Chandra* observations and improved Fe L line models for significantly under-ionized plasma are required to reveal the true nature of this candidate Fe-rich ejecta and its implications on the core-collapse nucleosynthesis and the details of the explosion mechanism.

The authors thank the referee for the careful review that help improve this work. We also thank K. Borkowski for providing us the updated atomic database and for the extensive discussion on the Fe L line fits in the low-ionization plasma. S.P. also thank S. Zhekov for the helpful discussion on the Fe L lines. S.P. and K.M. thank F. Bocchino for a useful discussion. This work was supported in part by Smithsonian Astrophysical Observatory under *Chandra* grant GO5-6063X.

REFERENCES

- Anders, E. & Grevesse, N. 1989, *Geochim. Cosmochim. Acta*, 53, 197
- Ballet, J. 2006, *AdSpR*, 37, 1902
- Bamba, A., Yamasaki, R., Ueno, M., & Koyama, K. 2003, *ApJ*, 589, 827

- Badenes, C., Borkowski, K. J., Hughes, J. P., Hwang, U., & Bravo, E. 2006, *ApJ*, 645, 1373
- Borkowski, K. J., Lyerly, W. J., & Reynolds, S. P. 2001, *ApJ*, 548, 820
- Cohen, R. S., Dame, T. M., Garay, G., Montani, J., Rubio, M., & Thaddeus, P. 1988, *ApJ*, 331, L95
- Dickey, J. M. & Lockman, F. J. 1990, *ARA&A*, 28, 215
- Ellison, D. C., Patnaude, D. J., Slane, P. O., Blasi, P., & Gabici, S. 2007, *ApJ*, 661, 879
- Gaensler, B. M., Haverkorn, M., Staveley-Smith, L., Dickey, J. M., McClure-Griffiths, N. M., Dickel, J. R., & Wolleben, M. 2005, *Science*, 307, 1610
- Ghavamian, P., Laming, J. M., & Rakowski, C. E., 2007, *ApJ*, 654, L69
- Gotthelf, E. V. & Wang, Q. D. 2000, *ApJ*, 532, L117
- Green, D. A. 2009, A Catalog of Galactic Supernova Remnants (2009 March version; Cambridge: Mullard Radio Astronomy Obs., Cavendish Laboratory), <http://www.mrao.cam.ac.uk/surveys/snrs>
- Hirayama, M., Nagase, F., Endo, T., Kawai, N., & Itoh, M. 2002, *MNRAS*, 333, 603
- Hughes, J. P., Rakowski, C. E., Burrows, D. N., & Slane, P. O. 2000, *ApJ*, 528, L109
- Hughes, J. P. 2001, in “Young Supernova Remnants”, The Eleventh Astrophysics Conference (Melville, NY: AIP), eds. S. S. Holt & U. Hwang, 419
- Hwang, U., Petre, R., Holt, S. S., & Szymkowiak, A. E. 2001, *ApJ*, 560, 742
- Hwang, U. & Laming, J. M. 2003, *ApJ*, 597, 362
- Kaaret, P. et al. 2001, *ApJ*, 546, 1159
- Kim, S., Staveley-Smith, L., Dopita, M. A., Freeman, K. C., Sault, R. J., Kesteven, M. J., McConnell, D. 1998, *ApJ*, 503, 674
- Kirshner, R. P., Morse, J. A., Winkler, P. F., & Blair, W. P. 1989, *ApJ*, 342, 260
- Manchester, R. N., Mar, D. P., Lyne, A. G., Kaspi, V. M., & Johnston, S. 1993a, *ApJ*, 403, L29
- Manchester, R. N., Staveley-Smith, L., & Kesteven, M. J. 1993b, *ApJ*, 411, 756
- Mathewson, D. S., Dopita, M. A., Tuohy, I. R., & Ford, V. L. 1980, *ApJ*, 242, L73
- Middleditch, J. & Pennypacker, C. R. 1985, *Nature*, 313, 659
- Morse, J. A., Smith, N., Blair, W. P., Kirshner, R. P., Winkler, P. F., & Hughes, J. P. 2006, *ApJ*, 644, 188

- Park, S., Kargaltsev, O., Pavlov, G. G., Mori, K., Slane, P. O., Hughes, J. P., Burrows, D. N., & Garmire, G. P. 2009, *ApJ*, 695, 431
- Petre, R., Hwang, U., Holt, S. S., Safi-Harb, S., & Williams, R. M. 2007, *ApJ*, 662, 988
- Reynolds, S. P. 1985, *ApJ*, 291, 152
- Reynolds, S. P. 1998, *ApJ*, 493, 375
- Reynolds, S. P. & Keohane, J. W. 1999, *ApJ*, 525, 368
- Russell, S. C. & Dopita, M. A. 1992, *ApJ*, 384, 508
- Serafimovich, N. I., Shibarov, Yu. A., Lundqvist, P., & Sollerman, J. 2004, *A&A*, 425, 1041
- Seward, F. D., Harnden, F. R., Jr., & Helfand, D. J. 1984, *ApJ*, 287L, 19
- Seward, F. D. & Harnden, F. R. 1994, *ApJ*, 421, 581
- Smith, R. K., Brickhouse, N. S., Liedahl, D. A., & Raymond, J. C. 2001, *ApJ*, 556, L91
- Townsley, L. K., Broos, P. S., Garmire, G. P., & Nousek, J. A. 2000, *ApJ*, 534, L139
- Townsley, L. K., Broos, P. S., Chartas, G., Moskalenko, E., Nousek, J. A., & Pavlov, G. G. 2002, *Nucl. Instrum. Methods Phys. Res. A*, 486, 716
- van der Heyden, K.J., Paerels, F., Cottam, J., Kaastra, J. S., & Branduardi-Raymont, G. 2001, *A&A*, 365, L254
- Williams, B. J. et al. 2008, *ApJ*, 687, 1054

Table 1. Best-Fit Model Parameters for the Arc Region.

Model	$N_{\text{H,LMC}}$ (10^{21} cm^{-2})	Γ	ν_{roll} (10^{17} Hz)	1 GHz Flux (mJy)	α	χ^2/ν
PL	$6.5^{+1.8}_{-1.5}$	$2.42^{+0.26}_{-0.23}$	-	-	-	39.8/31
SRCUT	$5.7^{+1.0}_{-0.9}$	-	$1.0^{+1.4}_{-0.4}$	0.19 ± 0.02	0.41^{a}	41.6/31
SRCUT	$5.7^{+1.0}_{-0.8}$	-	$2.1^{+4.7}_{-1.2}$	7^{b}	0.62 ± 0.01	41.1/31

^aThe radio spectral index α (where $S_\nu \propto \nu^{-\alpha}$) is fixed at $\alpha = 0.41$ as estimated for the entire SNR excluding the PWN (Manchester et al. 1993b).

^bThe 1 GHz flux is fixed at $f_{1\text{GHz}} = 7 \text{ mJy}$ as we estimate based on the 1.5 GHz image by Manchester et al. (1993).

Table 2. Best-Fit Spectral Parameters of SNR 0540–69.3.

Region	kT_{soft} (keV)	kT_{hard} (keV)	Γ	$n_{\text{e}}t_{\text{soft}}$ ($10^{10} \text{ cm}^{-3} \text{ s}$)	$n_{\text{e}}t_{\text{hard}}$ ($10^{10} \text{ cm}^{-3} \text{ s}$)	EM_{soft} (10^{57} cm^{-3})	EM_{hard} (10^{57} cm^{-3})	χ^2/ν
E ^a	$3.08^{+0.63}_{-0.92}$	-	-	$0.60^{+0.12}_{-0.08}$	-	$1.74^{+0.47}_{-0.27}$	-	64.8/55
	$1.72^{+1.63}_{-0.35}$	$3.20^{+2.55}_{-1.06}$	-	$3.37^{+3.03}_{-1.47}$	-	$0.37^{+0.13}_{-0.08}$	$1.59^{+0.52}_{-0.40}$	60.7/54
	$1.72^{+2.38}_{-0.69}$	-	2.23 ± 0.33	$3.46^{+6.16}_{-2.06}$	-	$0.30^{+0.16}_{-0.11}$	-	56.2/55
S ^b	$1.20^{+0.19}_{-0.60}$	-	-	$0.33^{+0.11}_{-0.07}$	-	$1.14^{+0.40}_{-0.23}$	-	32.9/33
SW	$0.74^{+0.10}_{-0.09}$	-	-	$5.27^{+3.43}_{-1.67}$	-	$2.32^{+0.35}_{-0.26}$	-	74.5/54
NW ^c	$0.90^{+0.16}_{-0.20}$	-	-	$6.30^{+9.90}_{-2.90}$	-	$6.33^{+3.96}_{-1.68}$	-	80.1/65
	$0.59^{+0.04}_{-0.04}$	$1.43^{+0.75}_{-0.43}$	-	$50.7^{+34.1}_{-17.6}$	< 0.08	$4.92^{+0.48}_{-0.63}$	$1.93^{+1.70}_{-0.85}$	66.3/68

Note. — $N_{\text{H,LMC}}$ is fixed at $6.0 \times 10^{21} \text{ cm}^{-2}$. Errors are with 90% confidence. For each region, one- and two-component plane-shock model fits are presented. The metal abundances are fixed at the LMC values, unless noted otherwise.

^aThe O and Ne abundances are varied in the one-shock model.

^bThe Fe abundance is varied while other elemental abundances are fixed at the LMC values.

^cThe metal abundances are varied in the one-shock model, while abundances are fixed at the LMC values in the two-shock model.

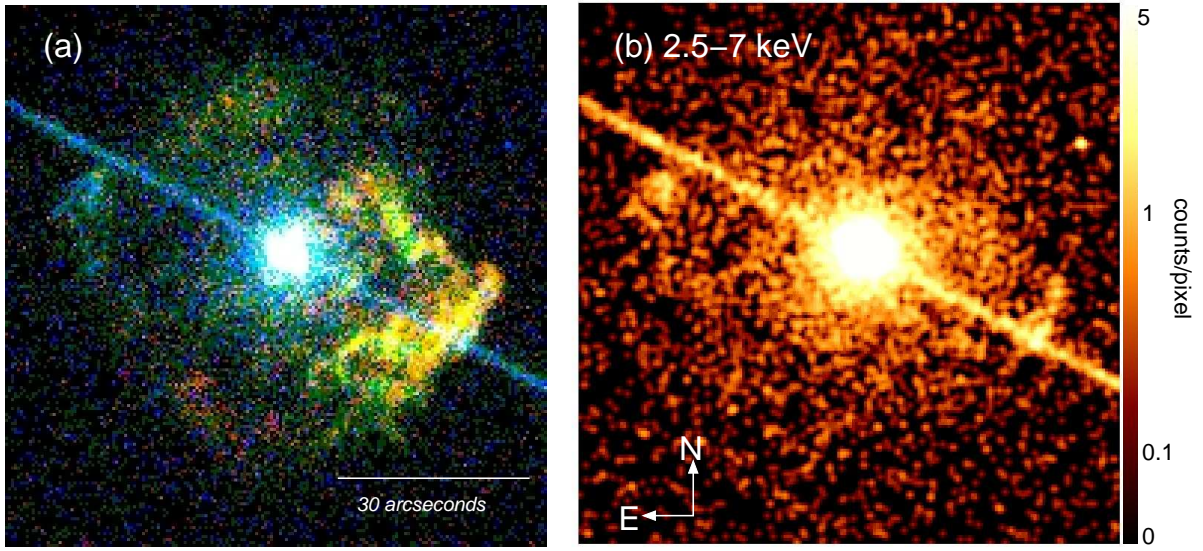


Fig. 1.— (a) An X-ray color image of SNR 0540–69.3 taken from the 114 ks *Chandra* observation. Red is 0.4–0.7 keV, green is 0.7–3 keV, and blue is 3–7 keV bands. Each subband image is binned into $0''.492$ pixels. (b) The hard band (2.5–7 keV) *Chandra* image of SNR 0540–69.3. The image is binned into $0''.492$ pixels. For the purposes of display, the image is smoothed by a Gaussian with $\sigma = 1''$. In both panels, the central pulsar and PWN are saturated to white to emphasize the faint filamentary features of the SNR.

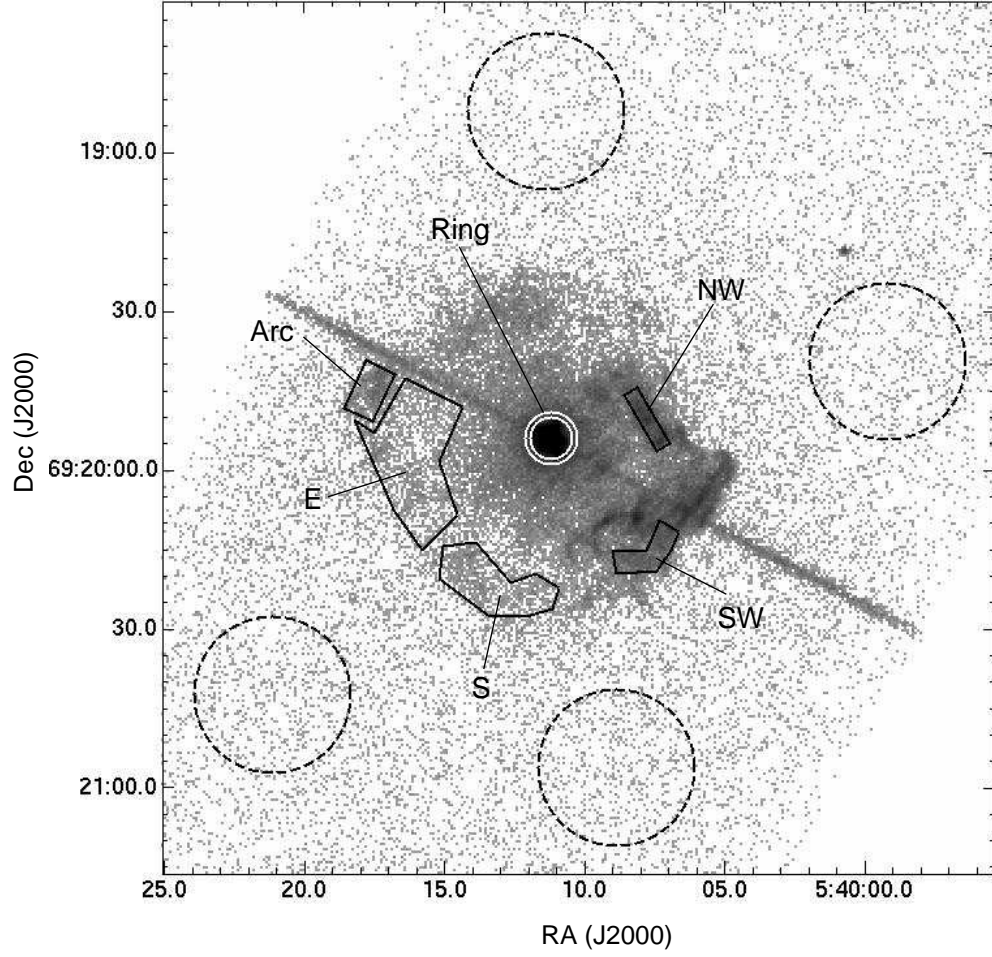


Fig. 2.— A grey-scale broadband (0.4–7.0 keV) *Chandra* image of SNR 0540–69.3. The image is binned into $0''.492$ pixels. Regions of our spectral analysis are marked. Dashed circles show regions where the background spectrum is estimated.

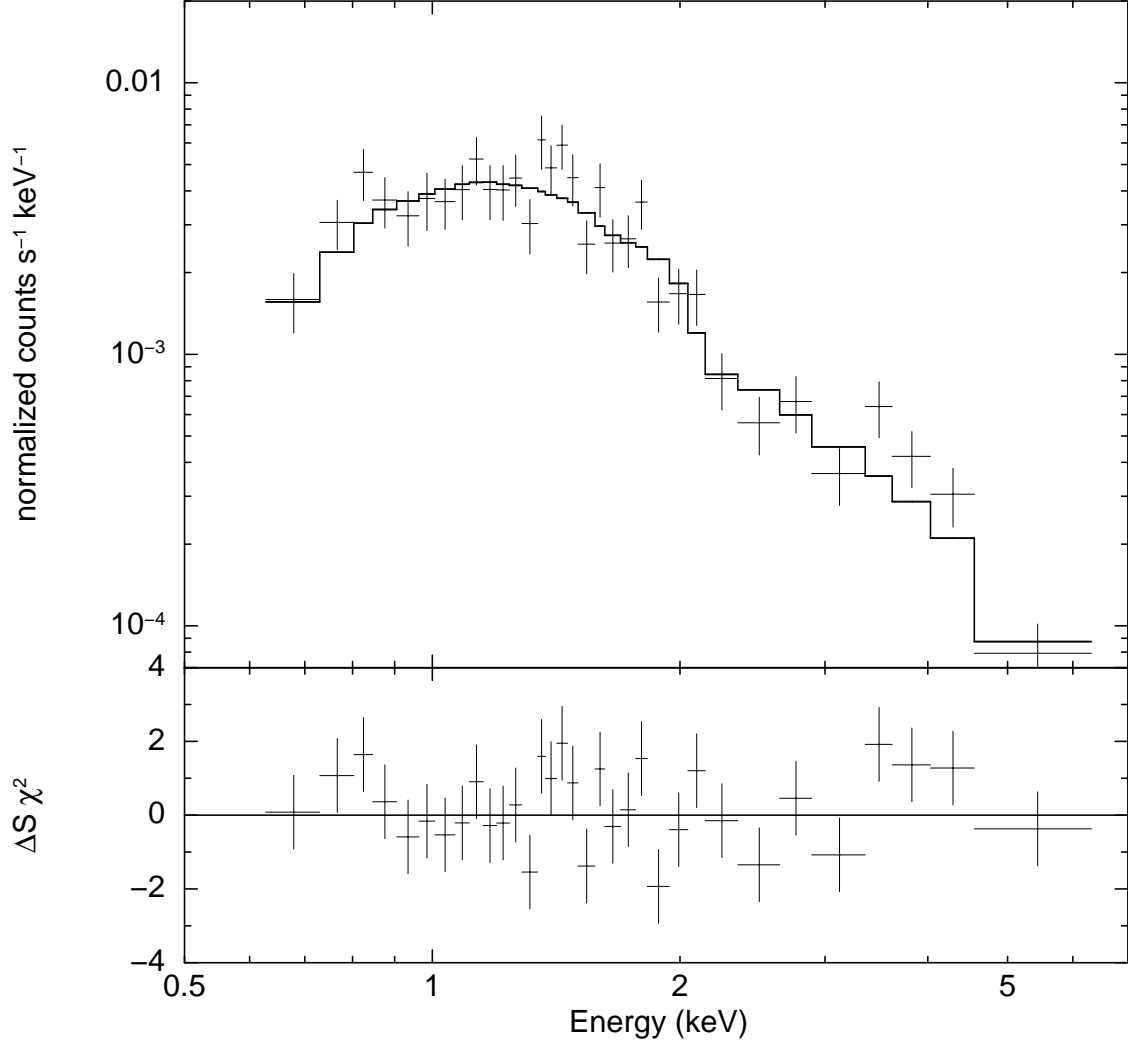


Fig. 3.— The *Chandra* ACIS spectrum of the Arc region. The best-fit PL model is overlaid. The lower panel shows the residuals from the best-fit model.

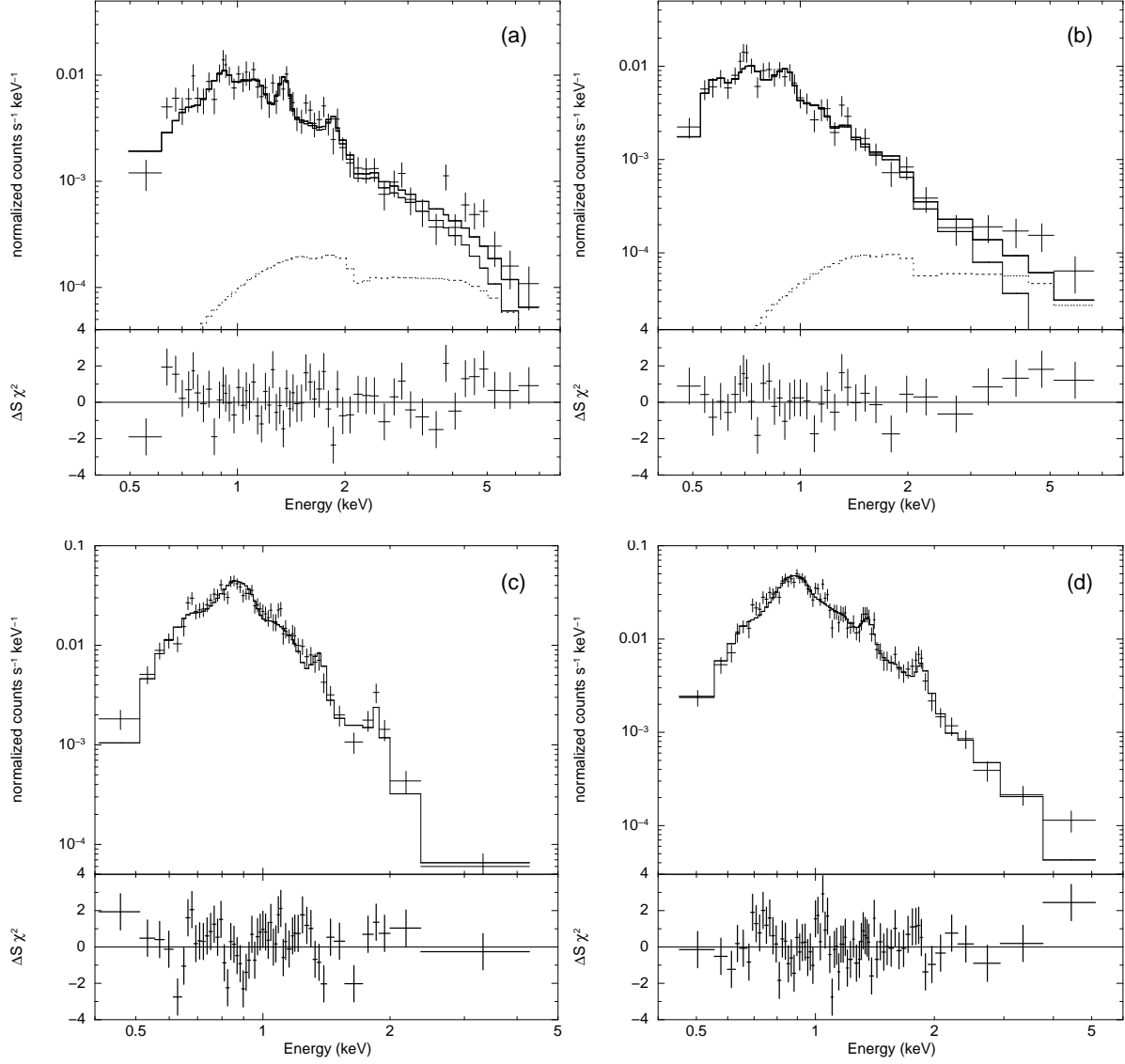


Fig. 4.— The *Chandra* ACIS spectrum of (a) the E, (b) the S, (c) the SW, and (d) the NW regions. In (a)-(d), the thick solid line shows the best-fit single plane-shock model. The lower panel shows the residuals from the best-fit model. In (a) and (b), the dotted line shows a PL model representing the estimated contamination by the scattered photons from the PWN.